





Article

Advanced Refinement of Geopolymer Composites for Enhanced 3D Printing via In-Depth Rheological Insights

Abrar Gasmi ^{1,*}, Christine Pélegris ¹, Ralph Davidovits ^{1,2}, Mohamed Guessasma ¹, Hugues Tortajada ³ and Florian Jean ⁴

¹ UPJV-LTI-UR 3899, 48 rue d'Ostende, 02315 Saint-Quentin, France; christine.pelegris@u-picardie.fr (C.P.)

² Institut Géopolymère, 02100 Saint-Quentin, France

³ UPJV-LTI-UR 3899, Avenue des Facultés-Le Bailly, 80025 Amiens, France

⁴ UPHF, CERAMATHS, Boulevard Charles de Gaulle, 59600 Maubeuge, France

* Correspondence: abrar.gasmi@u-picardie.fr

Abstract: The advancement of 3D printing technology has been remarkable, yet the quality of printed prototypes heavily relies on the rheological behavior of the materials used. This study focuses on optimizing geopolymer-based composite formulas to achieve high-quality 3D printing, with particular attention given to rheological analysis. Three metakaolins, Argical M1200s, Metamax, and Tempo M88, were used as alumino-silicate precursors for the preparation of the geopolymer binders. Rheological studies were conducted on viscosity, shear stress, and responses to oscillations in amplitude and frequency. The Tempo M88-based binder was identified as the most effective for the extrusion due to its optimal rheological properties. Subsequently, the study investigated the influence of the amount, up to 55%, and morphology of the fillers, comprising feldspar and wollastonite, on the rheology of the pastes. Also, the addition of Xanthan gum, a gelling agent in the geopolymer paste, was analyzed, revealing improved extrusion quality and more stable bead structures. Finally, a comprehensive comparison was carried out between two formulations chosen according to rheological observations, utilizing image sequences captured during 3D printing. This comparison highlighted the formulation that ensures structural stability, design accuracy, and minimized sagging. This study underscores the significance of geopolymer formula optimization, leveraging rheology as a pivotal tool to enhance 3D printing quality, thereby facilitating more precise and reliable applications of additive manufacturing.

Keywords: geopolymer-based composites; 3D printing; rheological characterization; rheological modifier additive



Citation: Gasmi, A.; Pélegris, C.; Davidovits, R.; Guessasma, M.; Tortajada, H.; Jean, F. Advanced Refinement of Geopolymer Composites for Enhanced 3D Printing via In-Depth Rheological Insights. *Ceramics* **2024**, *7*, 1316–1339. <https://doi.org/10.3390/ceramics7040087>

Academic Editor: Gilbert Fantozzi

Received: 23 July 2024

Revised: 29 August 2024

Accepted: 24 September 2024

Published: 27 September 2024



Copyright: © 2024 by the authors. Licensee MDPI, Basel, Switzerland. This article is an open access article distributed under the terms and conditions of the Creative Commons Attribution (CC BY) license (<https://creativecommons.org/licenses/by/4.0/>).

1. Introduction

In an age marked by escalating environmental concerns and the imperative for sustainable practices, the importance of green materials has become increasingly evident [1,2]. According to OECD data, the materials sector contributed 23% of global CO₂ emissions in 2023, with 19% stemming from cement, steel, and the production of chemicals [3]. Green materials, such as geopolymers, play a vital role in mitigating the environmental impact and enhancing quality of life [4,5]. Geopolymers, coined by Joseph Davidovits in the 1970s, offer a promising alternative to Portland cement, boasting eco-friendliness, versatility, and cost-effectiveness [6]. Their properties, including straightforward preparation and impressive physico-chemical attributes, have attracted significant attention from researchers [7,8].

However, the adoption of green materials alone cannot ensure ecological preservation; manufacturing processes also play a critical role. Additive manufacturing, or 3D printing, offers advantages such as reduced manpower and space requirements, leading to improved workforce efficiency and productivity [9]. Moreover, it enables customization opportunities, resulting in cost and time savings [10,11]. The synergy between green materials and additive manufacturing, exemplified by “extrusion-based geopolymer composites”,

represents a powerful force for environmental preservation and underscores technology's role in fostering sustainability for a greener future.

The success of 3D printing, particularly for complex geometries, is heavily dependent on the rheology of the paste used. Rheological properties such as viscosity, yield stress, and viscoelasticity are critical in ensuring that the material flows smoothly during extrusion, maintains its shape post-deposition, adheres to previous layers, and solidifies into a durable structure. A high recovery rate after shear is essential to minimize filament sagging during extrusion, preserving the structural integrity of the printed part. Optimizing viscosity and thixotropy is especially challenging: the paste must be fluid enough to extrude easily, yet regain its strength quickly after deposition to support subsequent layers. Thixotropy helps the material flow under stress and recover its viscosity once the stress is removed, ensuring precision in layer placement. At the same time, yield stress must be finely controlled to prevent the material from deforming under the weight of additional layers while still allowing flow during the extrusion process. These factors are crucial to overcoming common issues like poor interlayer adhesion or material collapse in intricate designs. Thus, achieving the right balance of rheological parameters is vital not only for successful 3D printing of complex shapes but also for ensuring the printed structure's mechanical stability once cured [12,13].

Zoude et al. [14] investigate how the mechanical properties of geopolymers vary based on their shaping and curing parameters. The findings reveal that the shaping method and curing conditions significantly impact the strength and durability of geopolymers. Understanding this connection is important for ensuring that printed geopolymer structures can achieve the necessary mechanical integrity for practical applications, especially in construction.

Franchin et al. [15] contributed to the understanding of rheological properties specific to 3D printing by focusing on geopolymer ink formulations. Their work aimed to balance printability with the functional performance of the material. However, the ink formulations in this study consisted solely of the geopolymer binder, without the inclusion of reinforcing materials. Despite producing highly porous ceramic lattices, up to 70% porosity, this work highlighted the need for further improvements in formulation to achieve more robust and functional prints.

In contrast, Ma et al. [16] emphasized the ability to fine-tune the mechanical properties of printed geopolymer structures through direct ink writing, achieving high spatial resolution. Their research demonstrated that the printing resolution and material composition could be adjusted to produce components with specific mechanical characteristics, such as stiffness or flexibility, making the technology suitable for creating highly customized parts. Pramanik et al. [17] examined the effect of extrusion parameters on the structural performance of geopolymer-based prints, reinforcing the notion that extrusion speed, nozzle geometry, and other processing factors must be finely tuned to achieve desired outcomes in printed parts. Other studies, such as those by Ricciotti et al. [18] and Wang et al. [19], have highlighted the evolution of extrusion-based 3D printing technologies using geopolymers. These works explored critical aspects such as the production process, printability, mix design, and early-age properties, alongside the sustainability benefits of using geopolymers. Geopolymers, known for their reduced carbon footprint compared to traditional cement, are positioned as an environmentally friendly material suitable for both construction and industrial applications.

Panda et al. [20] made significant strides in developing a one-part geopolymer mix designed specifically for 3D printing. This research provided insights into how material formulation can be optimized to allow for better shape retention during the printing process, ensuring that layers do not collapse or deform as subsequent layers are added. Their findings emphasize the importance of rheological control in ensuring the stability of 3D-printed layers.

Further studies on rheological behavior [21,22] have investigated critical factors such as shear-thinning behavior and shape retention during printing. These properties are

crucial for maintaining the dimensional accuracy of printed prototypes, particularly in intricate designs. Ma et al. [23] underscored the role of rheology modifiers in enhancing both the printability and mechanical properties of the final product. Additionally, the role of fillers and additives has been well-documented in the literature. For instance, fibers and other reinforcements [24] improve the rheological performance of geopolymer pastes, making them more suitable for extrusion. Gelling agents, such as Xanthan gum, have been studied for their ability to improve the structural integrity of printed components in various applications. Chen et al. [25] and Cofelice et al. [26] have also shown its ability to enhance the structural integrity of printed food components and other applications.

Finally, recent printability assessments [27,28] highlight various factors that influence printing efficiency and quality, including material composition and process parameters. Structural performance analyses [29,30] provide further insights into the mechanical properties and durability of 3D-printed geopolymers, which are essential for applications requiring strength and stability. Despite these advancements, a significant gap remains in quantitatively linking rheological properties to printability [31]. This presents an opportunity for further research to optimize extrusion-based geopolymer formulations for enhanced performance and broader application versatility.

The primary objective of this research is to enhance 3D printing technology by focusing on producing small, high-precision, and complex parts. As part of the GEOFAB project, these prototypes will be used in industrial applications, specifically for creating molding inserts used in thermoforming curved components in the aeronautical and automotive industries. Although the literature primarily focuses on large-scale construction applications and small-scale porous geopolymers or foams, this research targets heavily filled ceramic-like geopolymer composites to mitigate shrinkage, enhance mechanical properties, and investigate the effects of size distribution and morphology of the mineral filler elements.

The originality of this study lies in the development and optimization of geopolymer composites that are highly reinforced with mineral fillers. We aim to identify the optimal composition for high-quality extruded cord production and understand the influence of filler morphology and distribution. We began with a comprehensive assessment of different binders, including metakaolin variants (Tempozz M88, Metamax, and Argical M1200s) combined with potassium silicate, formulated through an alkaline process. Our selection was based on an in-depth analysis of rheological attributes.

After identifying the most suitable binder, we explored combinations filled up to 55% by weight with feldspar and wollastonite, chosen for their superior rheological performance. We also examined the effects of adding xanthan gum as a rheological modifier and gelling agent, focusing on its impact on rheological characteristics. Following the formulation of the optimal mix, we conducted comprehensive 3D printing trials to validate the functionality and performance of the geopolymer composite. These trials were essential to ensure that the material not only met the theoretical expectations derived from rheological testing but also performed reliably in practical applications.

2. Geopolymer-Based Composite Formulations

2.1. Material Characterization

The geopolymer binders were prepared from Woellner potassium silicate solution (Geosil 14517, Ludwigshafen, Germany) with a molar ratio of $\text{SiO}_2/\text{K}_2\text{O}$ of 1.7. To complement the silico-aluminate matrix synergistically with potassium silicate, we opted for metakaolin as the fundamental building block source. Three distinct types of metakaolins were examined: Tempozz M88 (Temcon, Germany/China), Argical M1200s (Imerys, Paris, France), and Metamax (KAMIN, Macon, GA, USA), referred to as M88, M1200s, MX, respectively, each presenting specific characteristics. This initial selection process was guided by an assessment of their rheological properties, aiming to identify the most suitable binder for our 3D printing objectives.

Following the identification of the optimal binder, the next step involved optimizing the filler ratio within the binder matrix. The incorporation of fillers serves to fine-tune the

material's characteristics, resulting in a final product with enhanced mechanical strength and reduced shrinkage. The chosen fillers include Feldspar IMX424 (Imerys, France) and Wollastonite 1250 mesh (Xatico, Luxembourg). Additionally, an extra step involved the introduction of a gelling agent, Xanthan gum, to the formulation.

In the scope of our investigation, supplementary experiments were conducted to further characterize our raw material powders. Particular emphasis was placed on examining the morphology of both our metakaolins and fillers, as depicted in Figures 1 and 2, respectively, utilizing Hitachi SU5000 (Hitachi High-Tech, Tokyo, Japan) and images acquired through Scanning Electron Microscopy (SEM). These SEM images offered invaluable visual insights, facilitating a detailed examination of the material morphology and enhancing our comprehension of microscopic properties. Following this, we proceeded to analyze the chemical composition of these constituents, as outlined in Table 1, employing Energy-Dispersive Spectroscopy (Thermo Scientific™ UltraDry EDS Detector, Waltham, MA, USA) to identify and quantify the elements present in the samples.

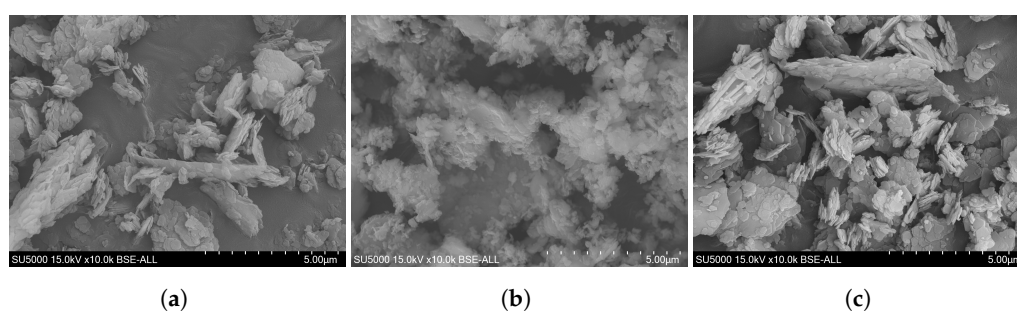


Figure 1. SEM micrographs of metakaolins: (a) M1200s, (b) M88, (c) MX.

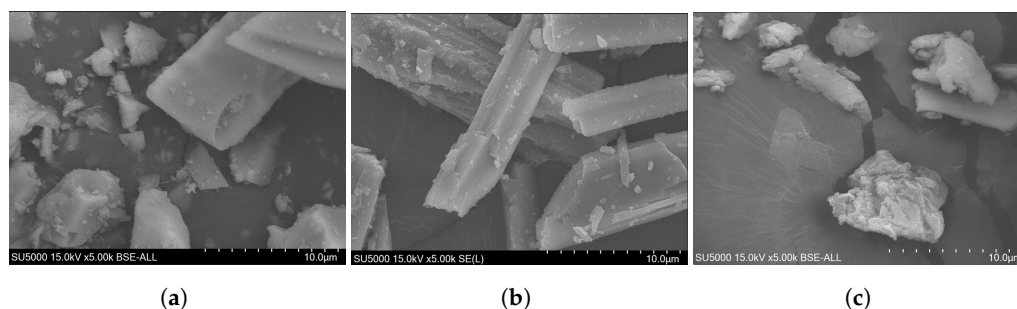


Figure 2. SEM micrographs of fillers: (a) Feldspar IMX424, (b) Wollastonite 1250 mesh, and additive: (c) Xanthan Gum.

Table 1. Chemical composition of constituent materials by weight (%).

Sample	O	Na	Al	Si	P	S	K	Ca	Ti	Fe	Zr	Mg	Cl
Tempozz M88	51.52	0.14	22.38	22.88	0.30	0.15	0.01	0.12	0.86	0.40	1.24	0.00	0.00
Metamax	52.40	0.27	19.36	20.79	0.65	0.42	0.00	0.00	0.95	0.19	4.66	0.28	0.04
Argical M1200s	51.11	0.08	18.52	22.07	0.60	0.15	0.70	0.12	0.52	1.24	4.03	0.84	0.01
Feldspar IMX424	52.20	0.25	4.41	38.50	0.00	0.00	4.65	0.00	0.00	0.00	0.00	0.00	0.00
Wollastonite 1250 mesh	48.99	0.00	0.28	20.16	0.00	0.00	0.00	30.27	0.00	0.00	0.00	0.31	0.00

The particle size distribution of metakaolins and fillers was thoroughly investigated through laser analysis using the Malvern Mastersizer 3000 (Malvern Panalytical, Malvern, UK), and the findings of this study are summarized and visually presented in Figure 3 alongside the median particle size data presented in Table 2.

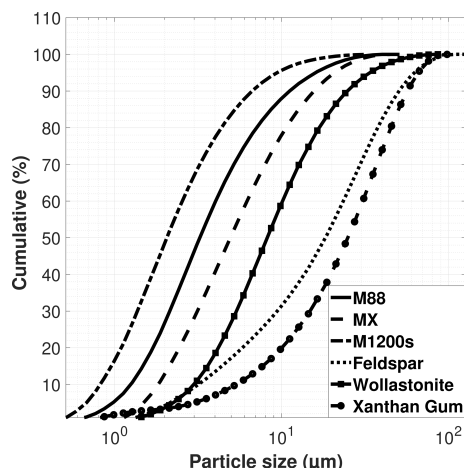


Figure 3. Particle size distribution of raw materials.

Finally, in-depth analyses were conducted to determine the specific surface area of metakaolins using Micromeritics TriStar II (Micromeritics Instrument, Norcross, GA, USA), revealing that M1200s exhibits the highest specific surface area, measured at 29.673 m²/g. Next, M88 follows with a surface area of 25.104 m²/g, and finally, Metamax displays a surface area of 22.864 m²/g. The specific surface areas of the metakaolins, along with those of the fillers, are summarized in Table 2 for a comprehensive comparison. These results have yielded crucial insights into the potential reactivity of the materials and their physical properties, thereby enhancing the database and characterizing our raw materials within the context of our study.

Table 2. Characterization of constituent materials.

Sample	Argical M1200s	Metamax	Tempozz M88	Feldspar IMX4224	Wollastonite 1250 Mesh
Median particle size (µm)	2	5	3	20	10
Specific surface Area (m ² /g)	29.673	22.864	25.104	3.851	51.523

2.2. Mix Design Method

The process of mixing geopolymer components involves several key steps to ensure thorough blending and uniform distribution. In the initial stage, M1200s, M88, or MX-metakaolin, along with potassium silicate, are combined in a molar ratio of K:Al = 1 [32]. This blending process is carried out using a Hei-Torque 200 mixer (Heidolph Instruments, Schwabach, Germany) at 350 rpm for 10 min to ensure thorough mixing of the base materials. These mixtures will be denoted as B-M1200s, B-M88, and B-MX, respectively.

Subsequently, a meticulous manual blending process is undertaken to ensure the uniform distribution of various fillers. Within our geopolymer-based composite paste formulations, which comprise either 40% or 55% of fillers added to 75 g of metakaolin-based binder, we explored four distinct options. Initially, ‘GP-F’ integrates 100% feldspar as the filler to understand its impact on the binder, while ‘GP-FW’ combines 80% feldspar with 20% wollastonite to evaluate the effect of incorporating a needle-shaped filler. Moreover, ‘GP-FWMax’, aimed at understanding the implications of adding more fillers, constitutes a blend of 80% feldspar and 20% wollastonite, transitioning from 40% to approximately 55% filler in the total weight of the geopolymer paste. Lastly, in the ‘GP-FWXg’ formula, we aimed to assess the influence of adding an additive to the formulation, where 79.5% of feldspar and 20% of wollastonite are combined with 0.5% of Xanthan gum additive to obtain 40% of fillers in the total weight of the geopolymer paste, as specified in Table 3. Following the filler mixing step, the mixture undergoes further blending for one minute at 200 rpm, with the duration of this final step varying depending on the additives used, typically ranging from 10 to 15 min. This systematic approach ensures the meticulous

preparation of geopolymer paste formulations tailored specifically for 3D printing, thereby guaranteeing reliability and consistency throughout the printing process.

Table 3. Proportions of fillers (%).

Formula	Feldspar/Fillers (%)	Wollastonite/Fillers (%)	Xanthan Gum/Fillers (%)	Total Weight Fillers (%)
GP-F	100	0	0	40
GP-FW	80	20	0	40
GP-FWMax	80	20	0	55
GP-FWXg	79.5	20	0.5	40

2.3. Rheological Protocol

The comprehension of rheological traits, particularly in materials such as geopolymer-based composites, involves introducing intentional disturbances to establish relationships between stimuli and responses [33]. In the realm of rheology, geopolymers often exhibit non-Newtonian behavior, viscoelasticity, and thixotropy [34,35].

The rheological characterization of geopolymer-based composite was carried out using the rotational Kinexus Lab+ rheometer (NETZSCH, Germany), employing vane geometry with a 25 mm diameter and 61 mm blade length. Measurements were consistently performed at 20 °C, with a 5 min material rest period when the upward plate reached the appropriate position. A pre-shear step is utilized in rheological experiments to standardize the rheological history of samples, ensuring a uniform initial state for all tests.

2.3.1. Shearing Tests

Continuous shear rheology involves applying a constant, steady shear rate to a material over a sustained period. This testing method is valuable for understanding the long-term behavior of materials, encompassing aspects such as flow properties, viscosity and shear-thinning behavior [36]. The first test focuses on the viscosity–shear rate relationship, highlighting variations in the viscosity of geopolymer composite material during 3D printing. To characterize our formulations, a shear rate ramp protocol ranging from 0.01 to 100 s^{−1} over a 10 min period was employed. The second test, known as the three interval-time-thixotropy (3ITT) test, involves a series of stages: an initial low shearing interval at 0.001 s^{−1} to assess the preserved geopolymer-based composite structure’s viscosity, followed by a phase of structural breakdown at elevated shear rates of 100 s^{−1}. Subsequently, the material returns to a low shear interval of 0.001 s^{−1} to observe the process of structural reformation.

2.3.2. Oscillatory Tests

Oscillatory shear rheology involves the periodic variation in shear stress or the rate of strain in shear flow kinematics over time [36]. The first test is the amplitude sweep, where a material undergoes increasing strain or deformation amplitudes at a fixed frequency [37]. To determine the transition of the material’s state from linear to non-linear viscoelastic regions, a stress sweep ranging from 0.001% to 100% was conducted, with a fixed frequency of 1 Hz for all samples [31,35,38]. The second test is the frequency sweep, a rheological testing technique characterizing the viscoelastic behavior of materials across a range of frequencies. The frequency range covers at least three decades, specifically from 0.1 Hz to 10 Hz, and the stress sweep was set at 0.01% to capture the material’s full behavioral spectrum [31].

2.4. Three-Dimensional Printing Protocol

In order to delve deeper into the correlation and validation of rheology test results, we proceeded with printing two distinct formulations to compare and validate our conclusions drawn from the previous section.

Our custom-built 3-axis gantry printer, developed in-house, is designed for building 3D-printed geopolymer-based composites. As shown in Figure 4, this printer can construct specimens up to 360 mm (Length) \times 240 mm (Width) \times 40 mm (Height). It operates using a piston extrusion mechanism powered by compressed air, reaching pressures up to 10 bars. This system is crucial for handling the viscous and shear-thinning properties of geopolymer pastes, which require controlled extrusion to maintain structural integrity [39]. Air pump pressure was carefully controlled between 1.5 and 4.5 bars, depending on the rheology of the mixture, to ensure consistent extrusion.

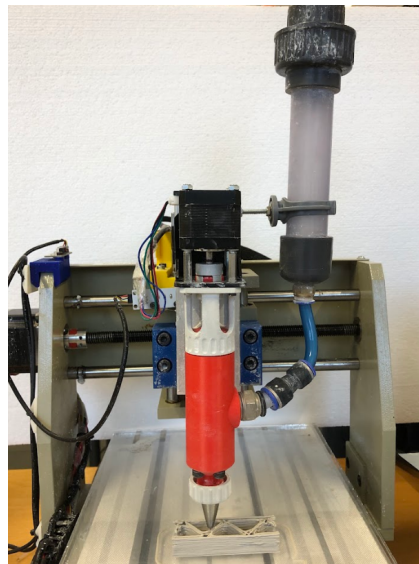


Figure 4. The 3D printing machine.

The extrusion system features a screw auger, allowing for precise control of both pressure and material flow rate. This level of control ensures consistent layer deposition and reduces common defects like air entrapment and inconsistent flow during printing. The auger's ability to handle varying material viscosities makes it particularly effective for geopolymer pastes, which often require fine-tuned adjustments during the extrusion process to balance flow and stability [40]. Compared to traditional piston systems, the screw auger imposes fewer mechanical constraints and reduces maintenance needs, enhancing long-term reliability and lowering operational costs. Additionally, its adaptability to complex geopolymer formulations, such as those with fillers or fibers, ensures even distribution of materials, which is critical for achieving uniform structural properties throughout the printed part. This flexibility is essential in ensuring the quality and performance of geopolymer composites in 3D printing applications [40].

This study employed nozzle diameters, spanning from 0.6 mm to 9.5 mm, to thoroughly assess the printability of geopolymer mixtures on a polypropylene surface. A range of shapes, including straight-wall, cylindrical and complex designs, were printed to evaluate extrusion behavior and structural integrity. Figure 5 presents the geometries after slicing, prepared using PrusaSlicer. These sliced models showcase the layer-by-layer breakdown of the structures, ready for 3D printing. The first test, involving a four-layer wall printed with a 9.5 mm nozzle (Figure 5a), focused on layer bonding and its effect on the stability of the first layer. Image analysis and MATLAB-based automation were used to standardize print quality assessment, monitoring geometric accuracy and the impact of layer deposition on factors such as deformation and sagging. The second test, using a 2 mm nozzle (Figure 5b), aimed to assess precision and stability when printing finer geometries, while also observing how curved trajectories influenced the elasticity of the formulations. Finally, the third test involved printing a complex geometry (Figure 5c) to study the impact of material flow on structural stability, particularly in intricate shapes. Additionally, we aimed to examine how printing at various angles impacted the deposition and quality of the

printed strand, focusing on how these orientations influenced the overall performance and consistency of the formulation. These tests provided a comprehensive understanding of geopolymer performance, optimizing both material composition and extrusion parameters to enhance 3D printing quality by addressing key factors like deformation, sagging, and structural stability [39,40].

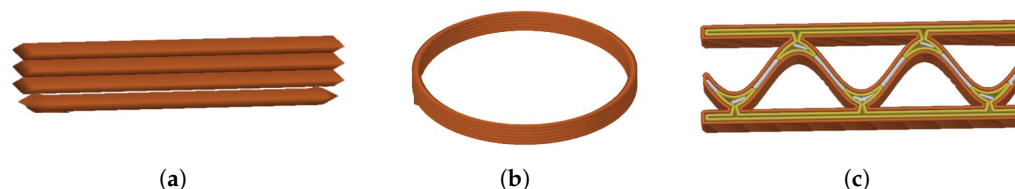


Figure 5. (a) Four-layer wall, (b) cylinder, (c) complex shape.

3. Results and Discussion

The initial crucial factor involves thoughtful material selection, encompassing binders (M88, M1200s, MX), fillers (Feldspar IMX424, Wollastonite 1250 mesh), and additive (Xanthan Gum), each contributing distinct rheological properties that must synergize in the formulation.

3.1. Rheometry Development for Extrusion-Based 3D Printing of Geopolymer Composites

3.1.1. Comparative Analysis of Binders: Rheological Behavior Evaluation

In this comparative analysis, we investigated three binders: B-M1200s, B-M88, and B-MX, each representing a combination of metakaolin (M1200s, M88, and MX) with potassium silicate. Each material presents distinct rheological characteristics, shedding light on their suitability for various applications, particularly in 3D printing.

Viscosity Shear Tests

B-M1200s stands out due to its remarkably high viscosity, which measures at 969.1 Pa.s, surpassing that of other examined binders (Figure 6). This distinct viscosity profile is attributed to B-M1200s's shorter reaction time, facilitating the formation of intricate polymeric structures. The particle size distribution of M1200s metakaolin is notably different, with a median size (d_{50}) of approximately 2 μm , the smallest among the compared metakaolins, as depicted in Table 2. A particle distribution implies more uniform particle sizing, fostering increased proximity between particles, as shown in Figure 1a. This proximity enhances interparticle attraction forces, including van der Waals and electrostatic forces, contributing significantly to the binder's overall viscosity [41]. Moreover, the viscosity of the binder is influenced by the size and shape of the dissolved oligomers. Longer and more entangled oligomers offer greater resistance to fluid shear [42]. As M1200s metakaolin exhibits the highest specific surface area of 29.673 m^2/g , as shown in Table 2, compared to other metakaolins, the interactions between molecules within the binder would be accentuated, enhancing fluid cohesion and consequently increasing viscosity [43].

Subsequently, B-M88 exhibits lower initial viscosity compared to B-M1200s, starting at approximately 80% lower, measuring at 180 Pa.s (Figure 6). It is well-established that an increased proportion of solids in metakaolin-based aluminosilicate slurries typically results in higher initial yield stress and apparent viscosity [44,45]. The viscosity contrast between B-M88 and B-M1200s can be attributed to several factors. Firstly, M88 metakaolin has a slightly higher d_{50} of 3 μm , as shown in Figure 3, and a lower specific surface area measured at 25.104 m^2/g compared to M1200s, as shown in Table 2. These differences reduce the impact of interparticle forces, leading to lower viscosity. Additionally, variations in the chemical composition of the two materials can alter particle interactions, further influencing viscosity. However, what truly distinguishes B-M88 is its rapid transition to fluidity, reaching a viscosity of 0.3 Pa.s at a shear rate of 100 s^{-1} . This notable shift can be attributed to the spherical particle shape, smooth surface, and ease of particle movement in the binder colloidal suspension, as illustrated in Figure 1b. Consequently, it facilitates swift alignment due to the impact of hydrodynamic forces and the untangling and alignment of polymer chains during flow [44]. As a result, the rate of viscosity reduction accelerates, enhancing the suitability of this binder for 3D printing applications.

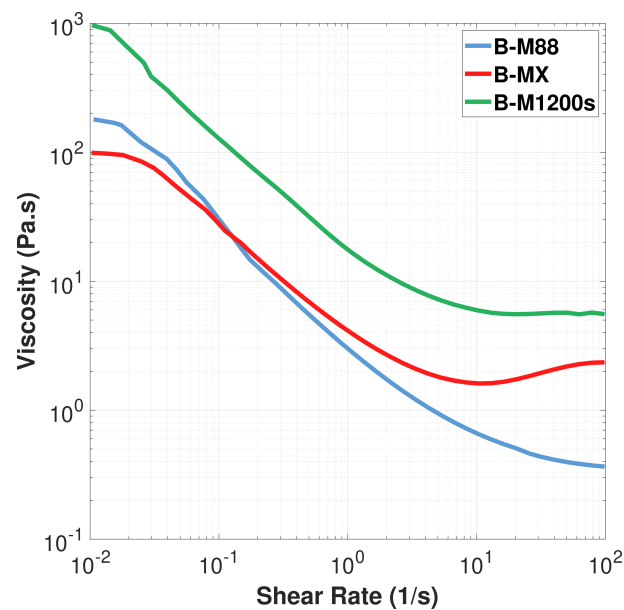


Figure 6. Shear viscosity tests of the binders.

B-MX displays an initial shear-thinning behavior, starting at 100 Pa.s and reaching 3.8 Pa.s at a shear rate of 1 s^{-1} . This lower viscosity is primarily attributed to its broader particle size distribution, approximately $5 \mu\text{m}$, compared to M1200s and M88 (Figure 3). The diverse particle sizes in MX metakaolin diminish the impact of interparticle forces, leading to reduced viscosity. Additionally, MX has the smallest specific surface area among the three metakaolins, measured at $22.864 \text{ m}^2/\text{g}$, as shown in Table 2, indicating less surface available for interparticle interactions. This combination of a broader particle size distribution and a smaller specific surface area accounts for B-MX having the lowest viscosity among the examined binders. An intriguing turning point is observed when the viscosity begins to increase slightly, transitioning into a shear-thickening behavior, ultimately reaching 2.35 Pa.s at 100 s^{-1} . This transition could be attributed to the rise in viscosity, likely driven by turbulent flow, as elevated shear rates can induce such effects [46].

The three binders exhibited shear-thinning behavior, attributed to the transformation of non-crosslinked polymer molecule shapes under shear stress [47]. Shear thinning is crucial for geopolymer-based composites in 3D printing, facilitating extrusion by reducing viscosity under applied shear stress and ensuring smoother flow [36,48].

Oscillation shear tests

Figure 7 illustrates rheological changes in geopolymer binders under shear strain, presenting storage modulus G' and loss modulus G'' . In rheology, the intersection point between G' and G'' represents the yield stress [23,49]. This yield stress indicates the point at which a material transitions from solid-like behavior to fluid-like behavior under stress. In the context of 3D printing, understanding the yield stress is crucial as it determines the minimum force required to initiate material flow through the printer nozzle, ensuring proper deposition of layers and overall print quality.

It is observed that all the binders exhibit a solid viscoelastic behavior, as evidenced by the fact that the storage component G' is greater than the loss component G'' . Moreover, they seem to have surpassed the point of intersection of the curves, indicating that they are beyond the transition region which refers to the crossover point where the material behavior shifts from being more elastic (able to hold shape) to more viscous (tending to flow) [50].

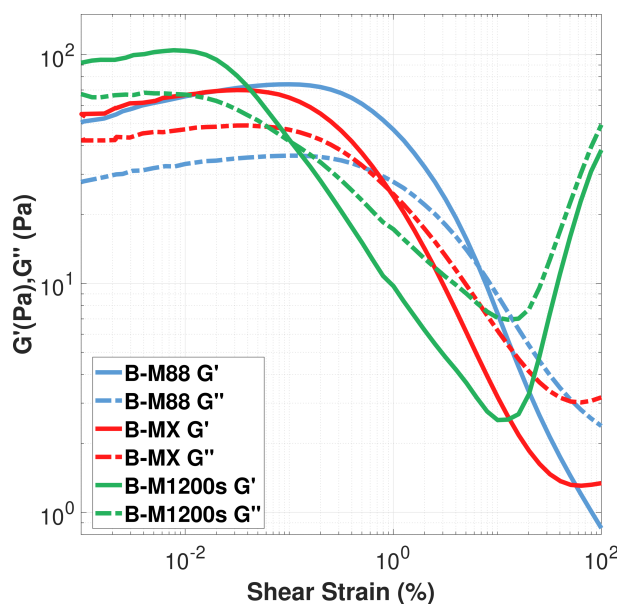


Figure 7. Oscillation amplitude sweeps of binders.

The order of G' values among the three binders, consistent with viscosity evaluation, highlights B-M1200s as distinctive with a G' of 94.1 Pa. This elevated storage modulus indicates heightened resistance to elastic deformation, underscoring M1200s' pivotal role in maintaining the material's solid viscoelastic structure. The yield stress, indicative of the point where the internal structure's network starts to break down, offers enhanced control at the onset of extrusion, preventing unintended material flow prior to intentional initiation. For B-M88, the determined yield stress was 8.1%, which was notably higher compared to B-MX at 1% and B-M1200s at 0.1%. This indicates that B-M88 necessitates a greater force during extrusion to initiate material flow. A high yield stress is not only associated with the material's ability to maintain its shape under external constraints but is crucial for ensuring precision and fidelity during the extrusion process, especially when printing successive layers. This property becomes essential in guaranteeing the deposited shape's accuracy. Researchers have linked yield stress to the material's capacity to maintain a desired structure under external forces, such as those induced by deposited geopolymer-based composite in subsequent layers or gravitational forces [51]. A material with a high yield stress exhibits a greater capacity to retain the desired shape after deposition.

The B-M1200s exhibit a distinctive behavior, particularly evident in amplitude oscillation data analysis at a 10% shear strain in Figure 7. Both the storage modulus G' and loss modulus G'' undergo a notable sequence of a sudden decrease followed by an increase. This phenomenon is attributed to the developing geopolymer network contributing to the elastic component, while stresses surpassing the elastic limit gradually disrupt the microstructural arrangement, facilitating the flow process. The observed response suggests a potential structural reorganization of the material.

It is noteworthy that the difference between the values of G' and G'' for the B-M88 is significantly higher than for the other binders, reaching a value of 26.38 Pa. This substantial difference may indicate the presence of a strongly crosslinked structure, similar to what occurs in a strongly bound dispersion. Furthermore, it may also suggest a low molecular weight distribution of crosslinked geopolymer chains. Consequently, this observation can be associated with a transition to a rubbery plateau in rheological behavior, highlighting a unique and strongly crosslinked geopolymer structure.

From a rheological perspective, B-M88 offers distinct performances. Viscosity tests reveal a rapid transition from the viscous to the liquid state, indicating enhanced pumpability of this binder. In amplitude sweep tests, B-M88 stands out with a high yield stress point, corresponding to a particularly broad linear viscoelastic region plateau. This signifies increased stability and the ability to maintain constant mechanical properties over an

extensive range of stresses. The moderate viscosity of B-M88 compared to that of B-M1200s allows for a higher filling capacity, which is the primary focus of this study. By increasing the loading capacity, we aim to enhance mechanical properties and reduce shrinkage. This approach leverages the versatility of B-M88 in accommodating higher filler content, contributing to the overall improvement of the material's performance and its suitability for 3D printing. These overall findings lead to the conclusion that the B-M88 is most suitable for ensuring good quality in the context of 3D printing. Consequently, for the remainder of this article, we will rely on M88 as the binder of choice and seek to optimize the filler ratio to maximize its performance.

3.1.2. Filler Optimization and Effect of Adding Gelling Agent: Rheological Behavior Evaluation

Introducing fillers to the geopolymer binder is essential for optimizing the 3D printing process, enabling precise control of rheology.

In this section, our aim is to optimize the filler ratio to incorporate into the B-M88. To achieve this goal, we conducted a comparative analysis of four different formulations of geopolymer-based composite paste, as detailed in Table 2, outlining the respective proportions.

Viscosity Shear Tests

In the investigation of the initial formula GP-F, the incorporation of feldspar particles into B-M88 demonstrates a significant impact on both viscosity and shear stress, as evidenced by Figure 8a,b. A substantial disparity is evident between the formulations B-M88 and GP-F, with viscosity increasing by 68%, from an initial 180 Pa.s to 566 Pa.s. Additionally, the yield stress, defined as the point where shear stress sharply increases relative to shear rate, marking the onset of substantial material flow [52], has risen by 77%, climbing from 2 Pa to 9 Pa. This effect is primarily attributed to the inclusion of feldspar particles, with a size of 20 μm , as depicted in Figure 3. The size of these feldspar particles further contributes to the increase in viscosity, with larger particles hindering molecular movement to a greater extent. Moreover, the angular morphology of the feldspar particles, as shown in Figure 2a, introduces geometric complexity into the binder matrix, impeding the movement of binder molecules and consequently elevating material viscosity. Simultaneously, molecular interactions, particularly hydrogen bonds, between binder components and feldspar particles enhance the material's structure, leading to an increase in yield stress [53,54]. Consequently, the addition of feldspar fillers not only alters particle morphology and size but also influences molecular interactions, resulting in a simultaneous rise in viscosity and shear stress.

The disparity in viscosity and shear stress is further accentuated with the introduction of wollastonite GP-FW formulation compared to GP-F, as demonstrated in Figure 8a,b. With the addition of wollastonite, the viscosity reaches 1001 Pa.s, surpassing the one without wollastonite by 43%, while the yield stress rises to 14.32 Pa, marking a 37% increase. The incorporation of wollastonite into the GP-F enables the modulation of B-M88 viscosity through multiple mechanisms. Wollastonite, known for its fibrous morphology characterized by elongated needle-like particles, as depicted in Figure 2b, acts as a physical barrier, hindering molecular mobility within the binder, with a d_{50} around 10 μm (Table 2). These obstacles disrupt fluidity, creating zones of resistance that need increased energy for binder molecules to navigate [55]. Moreover, wollastonite particles can interact with binder molecules, forming physical bonds such as van der Waals forces and chemical interactions such as hydrogen bonding. These interactions increase the material's structure, enhancing molecular cohesion [56]. Simultaneously, wollastonite has the capability to alter the molecular network structure within the binder by intertwining with binder molecules, resulting in a more complex structure and contributing to increased viscosity.

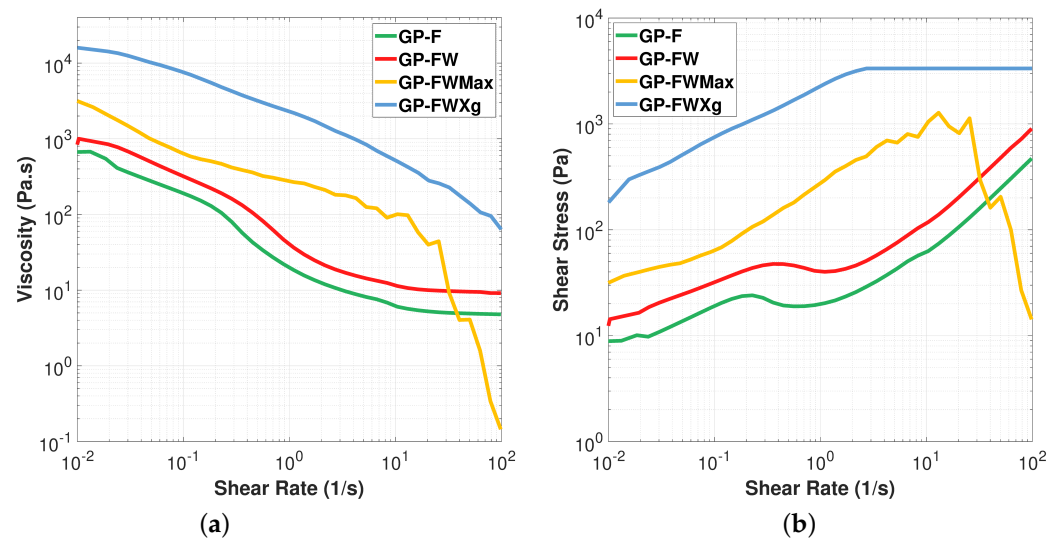


Figure 8. (a) Viscosity test; (b) shear stress test.

The GP-FWMax formula, containing 55% more fillers compared to GP-FW, exhibited a significant increase in viscosity, almost tripling to 2620 Pa.s and doubling in yield stress to 36.83 Pa. The heightened filler concentration led to a denser particle arrangement, impeding molecular movement and causing a surge in viscosity. At high shear rates, fluctuations in values were observed due to internal friction from irregular particles colliding, leading to interference, agglomeration, and increased internal friction. This instability resulted in non-constant viscosity and shear stress values, disrupting molecular movement consistency within the material.

Finally, the formulation incorporating the Xanthan gum additive GP-FWXg exhibited the most significant increase, registering an almost 90 times higher viscosity compared to B-M88, setting a record at 15,970 Pa.s, with a yield stress value of 181.4 Pa, according to Figure 8a,b. The addition of Xanthan gum to a geopolymer-based composite results in increased viscosity for various reasons. Xanthan gum, a polysaccharide extracted from bacteria, has the ability to form network structures in liquids. When introduced into a geopolymer, it acts as a thickening agent by creating a three-dimensional network [57,58]. This network hinders molecular movement, generating resistance to flow and increasing viscosity. Moreover, Xanthan gum is hygroscopic, and by absorbing water present in the geopolymer, it swells, causing an increase in volume and contributing to the viscosity rise. In summary, the thickening effect of Xanthan gum results from network formation and its water-absorbing ability, limiting the fluidity of the geopolymer and increasing viscosity [59]. Furthermore, Xanthan gum chains can interact with geopolymer molecules through hydrogen bonding [60]. These interactions strengthen the overall material structure, enhancing molecular cohesion, and consequently, increasing shear stress.

Table 4 displays the peak rheological values associated with the inclusion of B-M88, as extracted from Figure 8a,b. The Herschel–Bulkley model offers a more comprehensive description of the flow dynamics of non-Newtonian fluids, especially when the material exhibits yield stress behavior. This model is governed by three key parameters: the yield stress τ_0 , the consistency index K , and the flow index n . The yield stress τ_0 represents the stress that must be exceeded for the material to begin flowing, while K indicates the material's viscosity once the flow has started, and n describes the degree of shear-thinning or thickening behavior. A higher value of K reflects increased viscosity, and an n value of less than 1 indicates shear-thinning behavior [61]. To further investigate the non-Newtonian flow behavior, the Herschel–Bulkley model, as shown in Equation (1), was applied for modeling purposes [23], with R^2 representing the coefficient of determination. By fitting the experimental data using nonlinear regression, the parameters τ_0 , K , and n were identified, offering a precise quantification of the flow behavior across the observed shear rate range.

$$\tau = \tau_0 + K\dot{\gamma}^n \quad (1)$$

Table 4. Shear thinning coefficients for geopolymer formulas.

Geopolymer Formulas	Viscosity (Pa.s)	τ_0 (Pa)	K (Pa.s)	n	R^2
GP-F	566	9.01	4.624	0.912	0.993
GP-FW	1001	14.32	8.883	0.898	0.998
GP-FWMax	2620	36.83	277.223	0.588	0.988
GP-FWXg	15,970	181.41	2110.793	0.413	0.976

In the context of 3D printing, the manifestation of shear thinning, as indicated in Table 4, is evident when $n < 1$. Weak shear-thinning behavior is observed at n values close to 1 but still below it, typically indicating a moderate reduction in viscosity under shear. In contrast, strongly pronounced shear-thinning occurs at much lower n values, generally less than 0.5, where the material exhibits a significant reduction in viscosity when forced through the nozzle, facilitating flow [62,63]. Illustrated in Figure 8, all formulations display distinctive shear-thinning behavior, characterized by decreasing viscosity with escalating shear rate. This property signifies the fluid's ability to flow more readily under increased shear forces, which is crucial for successful extrusion in 3D printing. Table 4 further highlights that formulas with fillers GP-F and GP-FW exhibit n values of 0.912 and 0.898, respectively, indicating relatively weak shear-thinning behavior. Conversely, GP-FWMax and GP-FWXg display notably lower n values of 0.588 and 0.413, respectively, suggesting a more pronounced shear-thinning behavior, particularly in the case of GP-FWXg.

Three-interval thixotropy test

An insightful rheological analysis is facilitated by the three-interval thixotropy test (3ITT), applicable in either rotational or oscillatory modes. This test emulates extrusion-based printing through three distinct steps, as shown in Figure 9a,b: (1) a small shear rate in the linear viscoelastic region (LVR), mimicking the paste at rest in the 3D printing cartridge; (2) a high shear rate surpassing the flow point to replicate extrusion through the nozzle; and (3) a return to a small shear rate resembling the geopolymer paste's rest state after deposition.

The main goal is to evaluate the rapidity of solid-like behavior recovery, ensuring nozzle shape maintenance and sufficient modulus for precise printing and self-supporting structures. The second interval probes time-dependent viscosity, revealing thixotropic effects that may necessitate adjustments in printing parameters for consistent material flow [64]. For a geopolymer-based composite material, a satisfactory recovery parameter is defined as achieving 85% structural reformation. This level ensures that the layer stacking ability remains significantly dependent on the material's initial mechanical properties [65].

Analysis of Figure 10 and the data presented in Table 4 reveals a distinct trend in the thixotropic behavior across various geopolymer formulations. In the case of GP-F, the initial recovery response exhibits characteristic features: a notable peak viscosity of 924.1 Pa.s at 900 s is followed by a sharp decline to 88.51 Pa.s at 920 s, further decreasing to 24.18 Pa.s at 1000 s. Subsequently, there is a gradual increase, reaching 119.8 Pa.s at 1500 s. Drawing on observations by Mewis and Wagner [66], this sequence suggests a viscoelastic nature, with the initial peak indicating immediate elasticity, the rapid decrease signifying a transition to viscosity, and the subsequent rise, implying a return to elasticity, resulting in a 25.02% recovery rate.

In contrast to GP-F, the GP-FW formulation, incorporating wollastonite with a needle-like morphology, exhibits a distinct thixotropic behavior, as shown in Figure 10. Initially, viscosity sharply decreases to 36.92 Pa.s at 900 s, followed by an abrupt drop to 18.59 Pa.s at 920 s, and then a substantial increase to 69.56 Pa.s at 1000 s (Table 5). This pattern aligns with the ideal thixotropy classification [66], indicating initial thixotropy, followed by reversibility and subsequent inelastic behavior. The observed phenomena are attributed to complex interactions between wollastonite and feldspar particles during recovery, leading to flocculation or agglomeration [67,68].

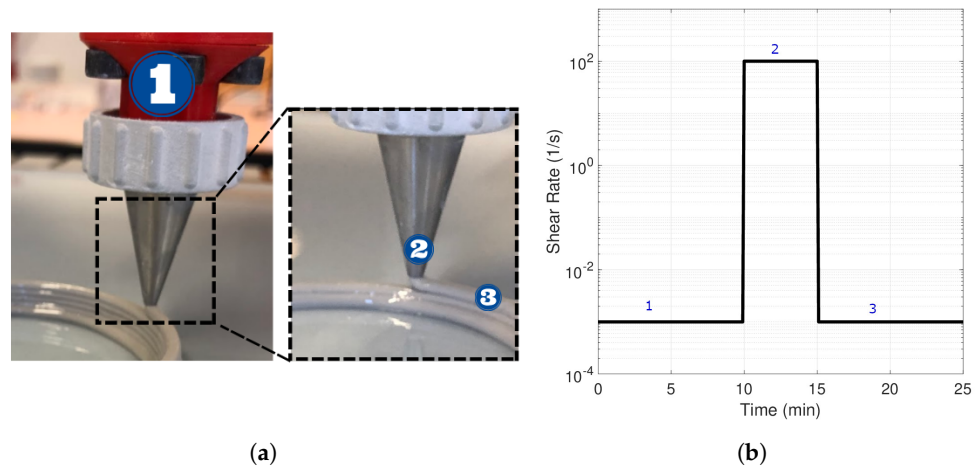


Figure 9. Correlation between thixotropy test and extrusion process: (a) extrusion process; (b) three intervals reproducing extrusion process.

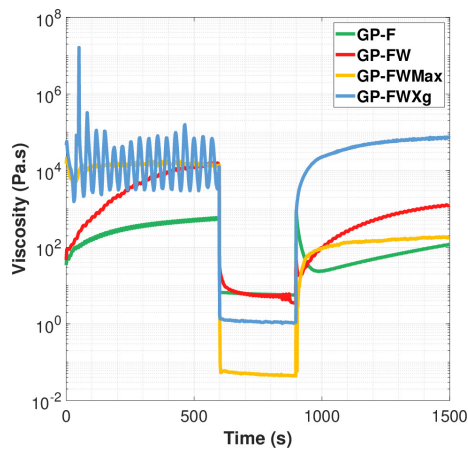


Figure 10. Three-step shear rate test.

Table 5. Three-step shear rate data.

Formulas	Viscosity (Pa.s)						Recovery (%)
GP-F	478.8	924.1	88.51	26.25	24.18	119.8	25.02
GP-FW	1.38×10^4	36.92	18.59	46.26	69.56	1.24×10^3	8.98
GP-FWMax	1.54×10^4	7.22	24.6	68	93	179	1.16
GP-FWXg	5.95×10^4	914	3.82×10^3	6.64×10^3	9.78×10^3	5.31×10^4	89.24
Time measurement (s)	500	900	920	950	1000	1500	

The GP-FWMax formula, reinforced with 55% of a mix of feldspar and wollastonite, results in a significant drop in the recovery rate to 1.16%, emphasizing the sensitivity of the material to specific filler combinations: a very high density can trap the molecules of the geopolymer, making their movement difficult and decreasing the material’s ability to regain its initial viscosity after being subjected to stress or deformation. Therefore, a low recovery rate can be directly attributed to a very high density resulting from a high filling ratio in the formulation. Figure 10 indicates a combination of viscoelastic and thixotropic responses, reinforcing the nuanced nature of the material’s behavior [69,70].

In the formula GP-FWXg, a distinctive observation emerges at the test’s initiation with a very low shear rate of 0.001 s^{-1} , revealing a sinusoidal viscosity pattern in Figure 10, indicative of substantial flocculation. This complex behavior arises from Xanthan gum’s ability to form a three-dimensional network, creating a gel-like structure in liquids [71]. At

extremely low shear rates during testing, Xanthan gum promotes molecular bonding, leading to the formation of denser aggregates or network structures [57]. These structures may demonstrate a sinusoidal response as they pass through the rheometer, reflecting variations in viscosity or deformation specific to this phase of the test. However, it is also possible that the sinusoidal pattern observed is partially due to noise from the rheometer itself, highlighting the need for careful interpretation of such behaviors at very low shear rates.

To precisely characterize the recovery rate, we calculated the average of all values collected during the initial test phase, revealing an initial viscosity of 5.95×10^4 Pa.s, as shown in Table 5. In the post-thixotropy test at 1500 s, a viscosity of 5.31×10^4 Pa.s was attained, resulting in an outstanding recovery rate of 89.24%, the highest among all formulations. This notable improvement can be attributed to Xanthan gum's incorporation, which is crucial for maintaining a uniform particle distribution in the geopolymer-based composite. By minimizing zones with low local concentrations, Xanthan gum enhances material consistency, especially during deformation and recovery phases [72]. Moreover, Xanthan gum's network structure creation when hydrated acts as a physical barrier between particles, preventing their proximity and floc formation [73].

Oscillation shear tests

The observations from Figure 11a,b indicate that the GP-F exhibits a liquid-like behavior throughout the entire range, with the viscous component G'' around 23.98 Pa exceeding the elastic component G' with a value of 14.78 Pa. This behavior is attributed to several factors related to the material's internal structure and component segregation [74]. Shear-induced phase transitions, triggered by high stresses, lead to molecular rearrangements and alterations in the geopolymer's microstructure [75]. Filler segregation, especially in feldspar, significantly impacts rheological properties, with clustered fillers hindering energy storage and increasing viscosity. This uneven distribution of fillers can impede the material's elastic properties, leading to energy dissipation and a rise in the viscous component. In applications such as 3D printing, where precise structural integrity is crucial, such behavior poses challenges.

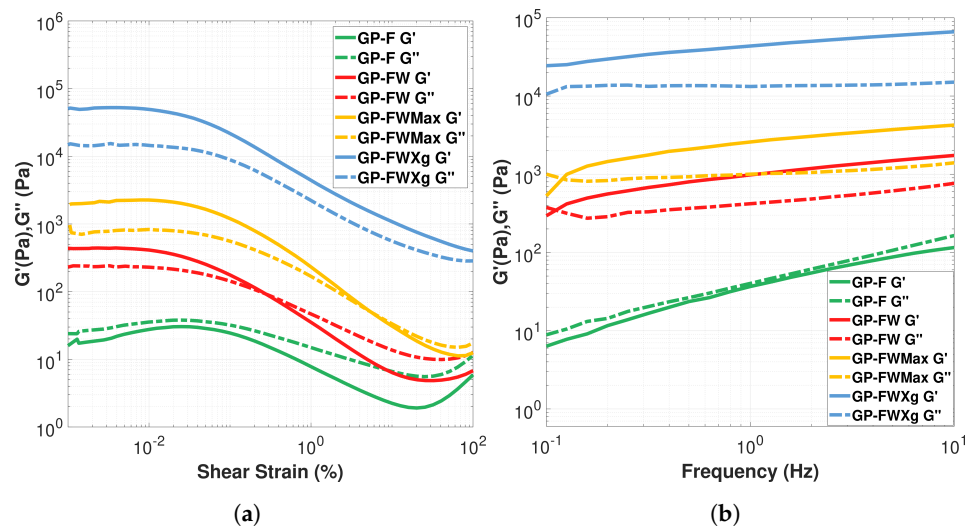


Figure 11. Oscillation tests: (a) amplitude sweeps; (b) frequency sweeps.

The addition of wollastonite GP-FW leads to significant changes, as evident in Figure 11a,b. A notable shift in the G''/G' ratio, causing curves to intersect in Figure 11a, indicates complex interactions and microstructural evolution. This effect is also observed in the frequency oscillation shown in Figure 11b. Initially, feldspar acts as a filler, inducing a viscous response in the geopolymer-based composite. However, introducing wollastonite needles brings substantial microstructural modifications. These needles reinforce the structure, promoting an elastic response through stronger bonds and a resilient three-dimensional network. This alteration greatly influences the mechanical behavior, increasing

elasticity with a yield stress of 96.54 Pa at 0.25% shear strain. The geopolymer's ability to recover its shape post-deformation is attributed to the robustness of needle interlacing. Consequently, the material exhibits elastic behavior under mechanical stress, highlighting its long-term structural stability, which is crucial for applications requiring resistance to repeated stresses.

A high amount of fillers in GP-FWMax results in more pronounced plateaus of G' and G'' , indicating a significant expansion in the material's linear viscoelastic behavior (LVE) range. The material now shows a broader zone of proportional and elastic response to applied shear stresses. At the same time, there is a notable increase in yield stress, rising from 0.25% to 62% in shear strain, as shown in Figure 11. This higher yield stress suggests increased resistance to permanent deformations or a greater stress threshold required to induce lasting changes in the material's structure [53]. These changes in rheological properties, observed with the addition of 55% feldspar and wollastonite, (Table 2), are attributed to their significant influence on the material's structure and behavior. The combined effect of these fillers enhances the geopolymer's resistance, leading to more pronounced plateaus and an elevated yield stress. These characteristics are essential in various applications where structural stability and mechanical resilience against permanent deformations are critical.

The dominance of G' over G'' in rheological results after adding Xanthan gum, GP-FWXg, is due to its unique molecular structure. Xanthan gum consists of linear polysaccharide chains with branched side chains, forming a robust three-dimensional network in water. These side chains act as junction points, creating a strong polymeric matrix [57]. This structural strength results in a prevalent elastic component G' in the rheological response. Under stress, the matrix undergoes elastic deformation, returning to its original shape afterward. Xanthan gum also influences the microstructure of the geopolymer-based composite, organizing particle dispersion in geopolymer composite matrix and enhancing their connection. Its thickening properties and gel-forming ability contribute to a cohesive three-dimensional structure, reinforcing resistance to stress. Intermolecular forces from its branched side chains establish a structured network, further enhancing elasticity. Intramolecular forces, such as hydrogen bonding, reinforce molecular cohesion [58]. Overall, Xanthan gum enhances the elastic properties of the geopolymer-based composite material, primarily due to its structured network and molecular cohesion.

Concluding the rheological study, the GP-FWXg appears to be the most suitable for 3D printing, as it exhibits the highest viscosity and a recovery rate exceeding 85%. It displays a gel-like behavior and demonstrates good dispersion. This combination of characteristics suggests that GP-FWXg possesses the necessary flow properties to ensure proper material deposition during printing while also maintaining structural integrity.

3.2. Printable Geopolymer-Based Composite Paste

The two formulations most suitable for 3D printing are GP-FXMax and GP-FWXg, owing to their high viscosities and substantial LVE plateaus. Their high viscosity allows for better control of material flow during printing, while their extended LVE plateaus indicate a broader zone of proportional and elastic response to applied stresses. The first step in the printing protocol involved printing a four-layer wall to assess the sagging of the initial layer, as shown in Figure 12.

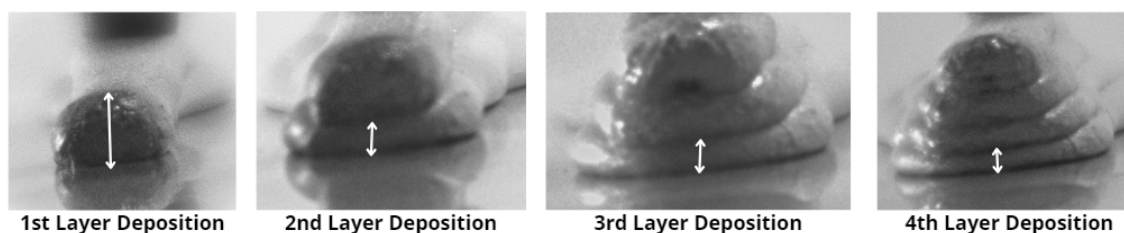


Figure 12. Sagging evolution of the 1st layer.

3.2.1. Three-Dimensional Printing of Geopolymer-Based Composite Formula “GP-FWMax”

Figure 13 quantitatively reveals a significant sagging in the first layer, originally designed as a circular shape with a height of 9.5 mm. It depicts the sagging rate of the first layer under its own weight, labeled “Layer1”, and the evolution of this rate under the deposition of subsequent layers, labeled “D.Layer n.”, (Figure 12).

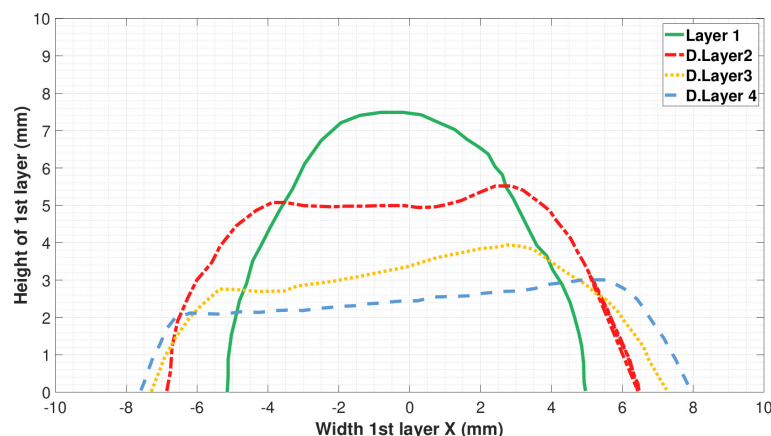


Figure 13. Shape of the first layer as a function of the deposition of subsequent layers.

The average height for the first layer measures 7.5 mm, a phenomenon explained by various physical and rheological mechanisms. The surface tension during extrusion plays a crucial role in material interaction with solid guide surfaces, influencing adhesion to the nozzle and mold walls. In instances of low surface tension and insufficient viscosity (2620 Pa.s in our case), poor adhesion may occur, leading to undesirable deformations. The material tends to spread beyond the intended shape, reducing the effective height of the cord. Post-extrusion, the geopolymer-based composite fails to fully regain its original shape, resulting in a permanent deformation and a 2 mm reduction in effective height. Additionally, continuous lateral flow contributes to a 10 mm increase in cord width. Gravity, notably pronounced due to our formula’s high loading, exerts a significant downward force on the material, as visible in Figure 13. This gravitational impact intensifies sagging rates, which reach 35% after the second layer deposition, then an average of 55% after the third layer deposition, and finally 70% after the fourth layer deposition. These findings underscore the material’s weight and gravitational force in cord sagging, attributed to a low recovery rate of approximately 1.16%, as shown in Figure 10. The geopolymer’s elastic nature, combined with nozzle extrusion, induces deformation under pressure, further reducing cord height compared to its non-elastic counterpart.

During the 3D printing of a cylinder with GP-FWMax, we observed various undesirable phenomena that had a significant impact on the extrusion process. One of these phenomena was the sporadic occurrence of air bubble explosions, as illustrated in Figure 14, specifically in the area-a of the piece. These air bubble explosions were detrimental to the smooth progress of the printing process and the quality of the finished object. Two major factors were identified as the root cause of this phenomenon. First and foremost, inadequate extrusion pressure was found to be a decisive factor. If the extrusion pressure is not properly adjusted, it can lead to fluctuations in the material flow as it is being extruded. In particular, excessive extrusion pressures can exert force on the air bubbles trapped within the material, causing them to be abruptly expelled and leading to bubble explosions within the geopolymer composite being extruded. Secondly, a lack of proper degassing during the printing process was also identified as a contributing factor. Air bubbles can form during printing if the material has not been adequately degassed beforehand. This degassing deficiency can result from difficulties in removing the trapped air within the material or from an inadequate chemical reaction that releases air during the extrusion.

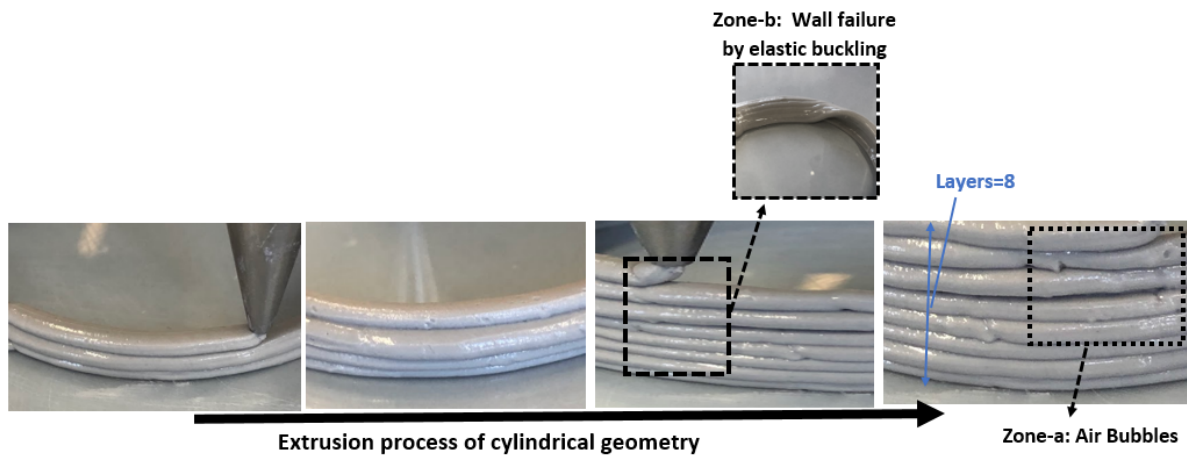


Figure 14. Critical issues for the extrusion process.

The presence of air bubbles during printing not only disrupted the workflow but also compromised the part’s quality, resulting in surface defects such as visible cavities and pores. Addressing air bubble formation is essential for ensuring high-quality 3D printing outcomes and maintaining the prototype’s intended functionality, particularly in critical roles such as sealing and mechanical strength.

While printing the final layer of the extrusion process, notably during the eighth and final layer, a mechanical phenomenon emerged (Figure 14, zone-b), characterized by instability and eventual structural collapse known as elastic buckling, a deformation occurring in thin structures under compressive loads [76]. This issue observed during the 3D printing of our geopolymers may be attributed to its low viscosity, approximately 2620 Pa·s, making the material excessively fluid and prone to difficulties in maintaining structural integrity. This fluidity, especially in vertical or overhanging areas, can result in sagging, deformation, and buckling, ultimately leading to unwanted distortions in the printed structure. The material’s reduced resistance to compression is a key factor contributing to this elastic buckling phenomenon.

The challenges associated with the recovery rate and post-printing deformation, arising from the remarkably low recovery rate of approximately 1% in our geopolymers-based composite, can significantly impact the 3D printing process. Adequate adhesion between successive layers is imperative for ensuring structural integrity. Inadequate adhesion, especially in vertical or overhanging regions, can lead to surface irregularities and defects (as illustrated in Figure 15, zone-a). Furthermore, such deficiencies in adhesion may culminate in the premature termination of the extrusion process due to a loss of stability. Specifically, this low recovery rate can result in vulnerable areas within the printed part, particularly susceptible to adhesion issues during the printing process (Figure 15, zone-b). Thus, addressing these issues is paramount for achieving high-quality and reliable 3D-printed complex design prototypes, requiring careful consideration and optimization of the printing parameters and material composition.



Figure 15. Formula printing issues.

3.2.2. Three-Dimensional Printing of Geopolymer-Based Composite Formula “GP-FWXg”

In comparison with the previous formula GP-FWMax, tests were conducted using the formulation containing Xanthan gum GP-FWXg, employing a 9.5 mm diameter nozzle to print a four-layer wall structure design analyzed through image sequences (Figure 12). Immediate improvements were evident, particularly in cord quality, with a significant reduction in sagging observed. While the previous formula exhibited a total sagging of 70%, the formula with Xanthan gum reduced this to approximately 40%. During the printing of the first cord, an average height of 8.5 mm was measured (Figure 16), resulting in a recovery rate of 90%, consistent with thixotropy tests (Table 4). The real revelation occurred during the printing of the second layer, where the influence of weight and gravity caused the first cord to deform, reducing its height to an average of 7.75 mm with a sagging rate of only 20%, significantly lower than observed previously.

This notable difference can be attributed to the extremely high viscosity of the Xanthan gum-containing formulation, promoting better-organized and more rigid interparticle interactions. These observations were further confirmed when adding the third and fourth layers, where we observed respective average sagging rates of 35% and 40% in height, as well as lateral expansion of 35% and 40% compared to the first layer, as indicated in Figure 16. These results clearly demonstrate the beneficial impact of adding Xanthan gum to the formulation, enhancing material cohesion, and significantly improving the stability of 3D-printed structures.

The second part of our experiments focuses on the printing of a cylinder under similar conditions to the previous section, using a 2 mm nozzle (Figure 17a). It is noteworthy that we have observed a marked improvement in cord quality, with a significant reduction in air bubble explosions on the surface, resulting in a visually more appealing texture. We printed the number of layers of the previous cylinder with GP-FWMax, and there was no buckling phenomenon, thanks to the solid viscoelastic behavior of the formulation.

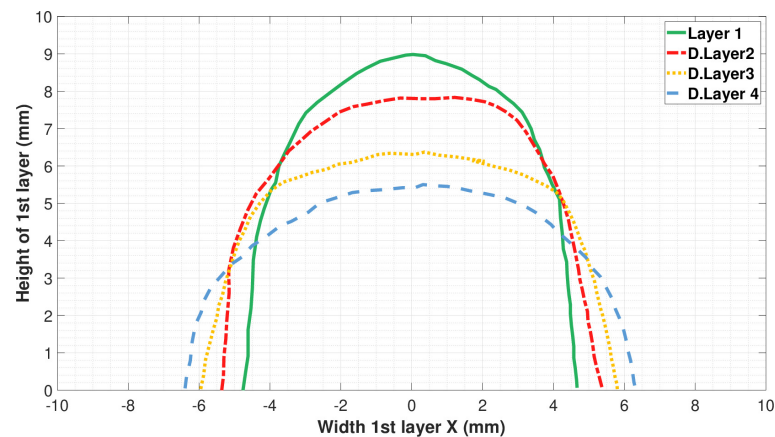


Figure 16. Shape of the first layer as a function of the deposition of subsequent layers.



Figure 17. Printing of cylindrical geometry: (a) printing with a nozzle of 2 mm; (b) printing with a nozzle of 0.6 mm.

Subsequently, we aimed to push the boundaries of our tests to determine the minimum nozzle diameter for printing. The cylinder design presented in Figure 17b was printed using a 0.6 mm nozzle under similar environmental conditions. We successfully printed up to 12 layers, utilizing two adjacent cords to enhance stability.

Even though we have achieved the correct formulation based on rheology, challenges remain, as precise parameter control is crucial, especially when dealing with complex geometries. This has been evident from the beginning with the phenomenon of zigzag patterns, also called “wavy patterns”, observed in Figure 18a and properly corrected in Figure 18b. In reality, an incorrect Z offset, i.e., the distance between the print nozzle and the print bed, can lead to an uneven printing surface, often manifested by irregular lines or ripples on the surface of the printed part. Thus, precise adjustment of the Z offset is essential to ensure high-quality 3D printing and minimize these visual defects.



Figure 18. Complex shape printing: (a) wavy patterns; (b) conforming part.

The SEM analysis, as shown in Figure 19, shows a cross-section of the 3D-printed geopolymer composite part (GP-FWXg), using a 0.6 mm diameter nozzle, as depicted in Figure 18b, which includes metakaolin Tempozz M88, potassium silicate, feldspar (d50 20 μm), wollastonite (d50 10 μm), and xanthan gum. The SEM images at varying scales (500 μm , 50 μm , and 10 μm) provide detailed insights into the microstructural integrity and performance of the printed material.

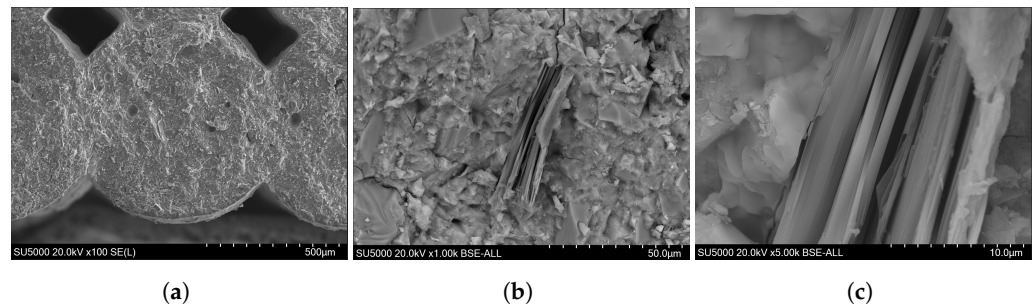


Figure 19. SEM of 3D-printed geopolymer composite part: (a) at 500 μm , (b) at 50 μm , and (c) at 10 μm .

At the 500 μm scale, Figure 19a reveals a generally homogeneous distribution of constituents throughout the composite. This uniformity indicates efficient mixing during the composite preparation, which is essential to prevent cold joints between the printed layers. The observed homogeneity suggests that the interaction between the geopolymer composite matrix and fillers during printing ensures continuous bonding, thus maintaining structural strength and coherence. The feldspar and wollastonite fillers are well dispersed, indicating an effective mixing process prior to printing. Additionally, the SEM images reveal that both the shape and the diameter of the strand were maintained accurately, indicating that the 3D printing process successfully adhered to the intended design specifications. The absence of cold joints highlights excellent cohesion between the printed layers, ensured by effective interaction between the binder and fillers during the printing process.

At the 50 μm scale, as shown in Figure 19b, the detailed distribution of feldspar and wollastonite fillers becomes apparent. Feldspar particles, with a median size of 20 μm ,

and wollastonite fibers, with a median size of 10 μm , are uniformly dispersed within the matrix. The directional flow of material through the 0.6 mm nozzle during printing aligns the wollastonite fibers parallel to the print direction. This alignment is advantageous as it enhances the mechanical properties of the composite along the direction of printing. The alignment is particularly beneficial for applications requiring anisotropic mechanical properties, where strength in a specific direction is crucial.

The 10 μm scale image, as shown in Figure 19c, reveals well-defined interfaces with excellent adhesion between the geopolymer matrix and the fillers. The distinct morphology of the wollastonite fibers, as evident at this scale, further confirms their alignment and interaction with the matrix. The fibers' needle-like structure provides reinforcement, improving the composite's resistance to cracking and deformation under load.

Xanthan gum plays a vital role in stabilizing the suspension of particles within the geopolymer composite matrix. Its presence ensures a uniform distribution of fillers, preventing the sedimentation and agglomeration that could lead to heterogeneous regions within the printed structure. This stabilization is indirectly observed through the consistent microstructural features across different scales, highlighting xanthan gum's efficacy in maintaining a stable mixture during the printing process.

4. Conclusions

In conclusion, our study highlights the pivotal role of particle size and morphology in shaping the rheological properties of geopolymer-based composites, particularly for 3D-printed parts with complex designs. The use of finer metakaolin emerged as a critical factor in increasing material viscosity, which guided the selection of optimal binders like B-M88. This binder is characterized by its high viscosity and notable linear viscoelastic behavior, which is crucial for maintaining cord quality, stability, and precision during printing. The strong viscoelasticity in the formulation preserves shape integrity, while reducing air bubble formation enhances surface smoothness—both essential for fine, stable printing. Additionally, the incorporation of a high content of feldspar and wollastonite as fillers, up to 55%, significantly enhanced the mechanical properties and dimensional stability of the geopolymer composites, underscoring their importance in achieving high-performance results. The incorporation of Xanthan gum into the geopolymer paste induced significant improvements in recovery rates and viscoelastic behavior, and these effects were specifically observed under specific stress conditions relevant to extrusion.

However, some limitations of this study must be acknowledged. The long-term stability of these formulations, particularly under varying environmental conditions (e.g., humidity or temperature), remains to be fully explored. Moreover, while the rheological enhancements facilitated the printing of complex geometries, further work is needed to fully characterize the limits of print resolution and structural fidelity in intricate designs, especially at smaller scales.

Future research will focus on addressing these limitations and expanding the scope of this study. Characterizing the thermal properties of the printed parts is essential, particularly for our industrial applications involving mold inserts, which requires high-temperature resistance, up to 800 $^{\circ}\text{C}$, and mechanical stability. Preliminary findings in this area have shown promise, but further investigation is necessary to confirm these results across a broader range of formulations and printing conditions. Additionally, we plan to leverage the rheological data obtained in computational fluid dynamics (CFDs) simulations to optimize the 3D printing process. These simulations will serve as predictive tools for anticipating material behavior post-extrusion and identifying potential issues early on, thus streamlining the printing workflow.

Author Contributions: Conceptualization, H.T.; methodology, A.G. and R.D.; validation, C.P. and M.G.; formal analysis, A.G. and F.J.; resources, H.T.; data curation, A.G. and F.J.; writing—original draft, A.G.; writing—review and editing, C.P., R.D. and M.G.; supervision, C.P., R.D. and M.G. All authors have read and agreed to the published version of the manuscript.

Funding: This work was realized under the GEOFAB project, funded by the region Hauts-de-France.

Institutional Review Board Statement: Not applicable.

Informed Consent Statement: Not applicable.

Data Availability Statement: Data are contained within the article.

Conflicts of Interest: The authors declare no conflicts of interest.

References

1. Hodžić, S.; Šikić, T.F.; Dogan, E. Green environment in the EU countries: The role of financial inclusion, natural resources and energy intensity. *Resour. Policy* **2023**, *82*, 103476. [[CrossRef](#)]
2. Satone, S.R.; Parbat, D.K.; Badar, A.M.; Varghese, V.P.; Satone, D.S.; Kawalkar, M.A. Application of green material on durability behaviour of green concrete. *Mater. Today Proc.* **2023**. [[CrossRef](#)]
3. Kowalski, P.; Legendre, C. *Raw Materials Critical for the Green Transition: Production, International Trade and Export Restrictions*; OECD: Paris, France, 2023.
4. Mahmoodi, O.; Siad, H.; Lachemi, M.; Dadsetan, S.; Şahmaran, M. Optimized application of ternary brick, ceramic and concrete wastes in sustainable high strength geopolymers. *J. Clean. Prod.* **2022**, *338*, 130650. [[CrossRef](#)]
5. Lu, C.; Zhang, Z.; Shi, C.; Li, N.; Jiao, D.; Yuan, Q. Rheology of alkali-activated materials: A review. *Cem. Concr. Compos.* **2021**, *121*, 104061. [[CrossRef](#)]
6. Davidovits, J. *Geopolymer Chemistry and Applications*; Institute Geopolymer: Saint-Quentin, France, 2008.
7. Shi, C.; Jiménez, A.F.; Palomo, A. New cements for the 21st century: The pursuit of an alternative to Portland cement. *Cem. Concr. Res.* **2011**, *41*, 750–763. [[CrossRef](#)]
8. Davidovits, J. Geopolymers: Ceramic-like inorganic polymers. *J. Ceram. Sci. Technol.* **2017**, *8*, 335–350.
9. Hegab, H.; Khanna, N.; Monib, N.; Salem, A. Design for sustainable additive manufacturing: A review. *Sustain. Mater. Technol.* **2023**, *35*, e00576. [[CrossRef](#)]
10. Dey, D.; Srinivas, D.; Panda, B.; Suraneni, P.; Sitharam, T. Use of industrial waste materials for 3D printing of sustainable concrete: A review. *J. Clean. Prod.* **2022**, *340*, 130749. [[CrossRef](#)]
11. Xiong, Y.; Tang, Y.; Kim, S.; Rosen, D.W. Human-machine collaborative additive manufacturing. *J. Manuf. Syst.* **2023**, *66*, 82–91. [[CrossRef](#)]
12. Roussel, N. Rheological requirements for printable concretes. *Cem. Concr. Res.* **2018**, *112*, 76–85. [[CrossRef](#)]
13. Botti, R.; Innocentini, M.; Faleiros, T.; Mello, M.; Flumignan, D.; Santos, L.; Franchin, G.; Colombo, P. Additively manufactured geopolymer structured heterogeneous catalysts for biodiesel production. *Appl. Mater. Today* **2021**, *23*, 101022. [[CrossRef](#)]
14. Zoude, C.; Prud'homme, E.; Johannes, K.; Gremillard, L. The Mechanical Properties of Geopolymers as a Function of Their Shaping and Curing Parameters. *Ceramics* **2024**, *7*, 873–892. [[CrossRef](#)]
15. Franchin, G.; Scanferla, P.; Zeffiro, L.; Elsayed, H.; Baliello, A.; Giacomello, G.; Pasetto, M.; Colombo, P. Direct ink writing of geopolymeric inks. *J. Eur. Ceram. Soc.* **2017**, *37*, 2481–2489. [[CrossRef](#)]
16. Ma, S.; Fu, S.; Zhao, S.; He, P.; Ma, G.; Wang, M.; Jia, D.; Zhou, Y. Direct ink writing of geopolymer with high spatial resolution and tunable mechanical properties. *Addit. Manuf.* **2021**, *46*, 102202. [[CrossRef](#)]
17. Pramanik, A.; Subhani, T.; Yun, T.S.; Nagesh, R.; Ramakrishna, S. Exploring the Structural Performance of 3D-Printed Geopolymer-based Architectural Components. *Mater. Today Commun.* **2021**, *27*, 102382.
18. Ricciotti, L.; Apicella, A.; Perrotta, V.; Aversa, R. Geopolymer materials for extrusion-based 3D-printing: A review. *Polymers* **2023**, *15*, 4688. [[CrossRef](#)]
19. Jia, D.; He, P.; Wang, M.; Yan, S.; Jia, D.; He, P.; Wang, M.; Yan, S. Geopolymers and Their Matrix Composites: A State-of-the-Art Review. *Geopolymer Geopolymer Matrix Compos.* **2020**, *311*, 7–34.
20. Panda, B.; Singh, G.V.P.B.P.; Unluer, C.; Tan, M.J. Synthesis and characterization of one-part geopolymers for extrusion based 3D concrete printing. *J. Clean. Prod.* **2019**, *220*, 610–619.
21. Kovářik, T.; Hájek, J.; Hervert, T.; Deshmukh, K.; Pola, M.; Jansa, Z.; Beneš, J.; Svoboda, M. Silica-based geopolymer spherical beads: Influence of viscosity on porosity architecture. *Cem. Concr. Compos.* **2021**, *124*, 104261. [[CrossRef](#)]
22. Amorim, P.; d'Ávila, M.; Anand, R.; Moldenaers, P.; Van Puyvelde, P.; Bloemen, V. Insights on shear rheology of inks for extrusion-based 3D bioprinting. *Bioprinting* **2021**, *22*, e00129. [[CrossRef](#)]
23. Ma, S.; Fu, S.; Yang, T.; Li, K.; Chen, G.; Dong, Q.; He, P.; Sun, Z.; Duan, X.; Jia, D.; et al. Unveiling the critical role of rheology modifiers in additive manufacturing of geopolymers and their mechanical properties. *Addit. Manuf.* **2023**, *78*, 103826. [[CrossRef](#)]
24. Ilcan, H.; Sahin, O.; Kul, A.; Ozcelikli, E.; Sahmaran, M. Rheological property and extrudability performance assessment of construction and demolition waste-based geopolymer mortars with varied testing protocols. *Cem. Concr. Compos.* **2023**, *136*, 104891. [[CrossRef](#)]
25. Chen, Y.; Zhang, M.; Sun, Y.; Phuhongsung, P. Improving 3D/4D printing characteristics of natural food gels by novel additives: A review. *Food Hydrocoll.* **2022**, *123*, 107160. [[CrossRef](#)]
26. Cofelice, M.; Messia, M.C.; Marconi, E.; Cuomo, F.; Lopez, F. Effect of the xanthan gum on the rheological properties of alginate hydrogels. *Food Hydrocoll.* **2023**, *142*, 108768. [[CrossRef](#)]

27. Gonçalves, N.P.; Olhero, S.M.; Labrincha, J.A.; Novais, R.M. 3D-printed red mud/metakaolin-based geopolymers as water pollutant sorbents of methylene blue. *J. Clean. Prod.* **2023**, *383*, 135315. [[CrossRef](#)]
28. Chen, W.; Pan, J.; Zhu, B.; Ma, X.; Zhang, Y.; Chen, Y.; Li, X.; Meng, L.; Cai, J. Improving mechanical properties of 3D printable 'one-part' geopolymer concrete with steel fiber reinforcement. *J. Build. Eng.* **2023**, *75*, 107077. [[CrossRef](#)]
29. Asghar, R.; Khan, M.A.; Alyousef, R.; Javed, M.F.; Ali, M. Promoting the green construction: Scientometric review on the mechanical and structural performance of geopolymer concrete. *Constr. Build. Mater.* **2023**, *368*, 130502. [[CrossRef](#)]
30. Shilar, F.A.; Ganachari, S.V.; Patil, V.B.; Bhojaraja, B.; Khan, T.Y.; Almakayeel, N. A review of 3D printing of geopolymer composites for structural and functional applications. *Constr. Build. Mater.* **2023**, *400*, 132869. [[CrossRef](#)]
31. Arunothayan, A.R.; Nematollahi, B.; Khayat, K.H.; Ramesh, A.; Sanjayan, J.G. Rheological characterization of ultra-high performance concrete for 3D printing. *Cem. Concr. Compos.* **2023**, *136*, 104854. [[CrossRef](#)]
32. Davidovits, J. *Geopolymer Chemistry and Applications*, 5th ed.; Institut Géopolymère, Geopolymer Institute: Saint-Quentin, France, 2020; Chapter 21.
33. Sabbatini, A.; Vidal, L.; Pettinari, C.; Sobrados, I.; Rossignol, S. Control of shaping and thermal resistance of metakaolin-based geopolymers. *Mater. Des.* **2017**, *116*, 374–385. [[CrossRef](#)]
34. Favier, A. *Mécanisme de Prise et Rhéologie de Liants Géopolymères Modèles*. Ph.D. Thesis, Université Paris-Est, Paris, France, 2013.
35. Keskin-Topan, Y.; Bessaies-Bey, H.; Petit, L.; Tran, N.C.; d'Espinose de Lacaillerie, J.B.; Rossignol, S.; Roussel, N. Effect of maximum packing fraction of powders on the rheology of metakaolin-based geopolymer pastes. *Cem. Concr. Res.* **2024**, *179*, 107482.
36. Zhang, J.; Tuohey, J.; Amini, N.; Morton, D.A.; Hapgood, K.P. 3D printing of customised particles for powder rheology, mixing and segregation study. *Powder Technol.* **2023**, *425*, 118576. [[CrossRef](#)]
37. Dávila, J.; d'Ávila, M. Rheological evaluation of Laponite/alginate inks for 3D extrusion-based printing. *Int. J. Adv. Manuf. Technol.* **2019**, *101*, 675–686.
38. Yan, D.; Chen, S.; Zeng, Q.; Xu, S.; Li, H. Correlating the elastic properties of metakaolin-based geopolymer with its composition. *Mater. Des.* **2016**, *95*, 306–318. [[CrossRef](#)]
39. Hass, L.; Bos, F. Bending and pull-out tests on a novel screw type reinforcement for extrusion-based 3D printed concrete. In Proceedings of the Second RILEM International Conference on Concrete and Digital Fabrication: Digital Concrete 2020, Eindhoven, The Netherlands, 6–8 July 2020; Springer: Berlin/Heidelberg, Germany, 2020; pp. 632–645.
40. Sanjayan, J.; Jayathilakage, R.; Rajeev, P. Vibration induced active rheology control for 3D concrete printing. *Cem. Concr. Res.* **2021**, *140*, 106293. [[CrossRef](#)]
41. Tanner, R.I. *Engineering Rheology*; Oxford University Press: Oxford, UK, 2000; Volume 52.
42. Graessley, W.W. The entanglement concept in polymer rheology. In *The Entanglement Concept in Polymer Rheology*; Springer: Berlin/Heidelberg, Germany, 2005; pp. 1–179.
43. Barnes, H.A.; Hutton, J.F.; Walters, K. *An Introduction to Rheology*; Elsevier: Amsterdam, The Netherlands, 1989; Volume 3.
44. Rovnaník, P.; Rovnanikova, P.; Vyšvařil, M.; Grzeszczyk, S.; Janowska-Renkas, E. Rheological properties and microstructure of binary waste red brick powder/metakaolin geopolymer. *Constr. Build. Mater.* **2018**, *188*, 924–933. [[CrossRef](#)]
45. Romagnoli, M.; Leonelli, C.; Kamse, E.; Gualtieri, M. Rheology of geopolymer by DOE approach. *Constr. Build. Mater.* **2012**, *36*, 251–258.
46. Ewoldt, R.H.; Johnston, M.T.; Caretta, L.M. Experimental challenges of shear rheology: How to avoid bad data. In *Complex Fluids in Biological Systems: Experiment, Theory, and Computation*; Springer: Berlin/Heidelberg, Germany, 2015; pp. 207–241.
47. Guy, C.; Jean-Louis, G.; Nicolas, H. *Initiation à la Rhéologie (4 Éd.): Bases Théoriques et Applications Expérimentales*; Lavoisier: Paris, France, 2014.
48. de Andrade, R.; Paim, T.C.; Bertaco, I.; Naasani, L.S.; Buchner, S.; Kovářík, T.; Hájek, J.; Wink, M.R. Hierarchically porous bioceramics based on geopolymer-hydroxyapatite composite as a novel biomaterial: Structure, mechanical properties and biocompatibility evaluation. *Appl. Mater. Today* **2023**, *33*, 101875. [[CrossRef](#)]
49. Maldonado-Rosas, R.; Tejada-Ortigoza, V.; Cuan-Urquizo, E.; Mendoza-Cachú, D.; Morales-de La Pena, M.; Alvarado-Orozco, J.M.; Campanella, O.H. Evaluation of rheology and printability of 3D printing nutritious food with complex formulations. *Addit. Manuf.* **2022**, *58*, 103030. [[CrossRef](#)]
50. Malkin, A.; Kulichikhin, V.; Ilyin, S. A modern look on yield stress fluids. *Rheol. Acta* **2017**, *56*, 177–188. [[CrossRef](#)]
51. Liu, Z.; Bhandari, B.; Prakash, S.; Mantihal, S.; Zhang, M. Linking rheology and printability of a multicomponent gel system of carrageenan-xanthan-starch in extrusion based additive manufacturing. *Food Hydrocoll.* **2019**, *87*, 413–424. [[CrossRef](#)]
52. Nguyen, Q.D.; Akroyd, T.; Kee, D.C.D.; Zhu, L. Yield stress measurements in suspensions: An inter-laboratory study. *Korea-Aust. Rheol. J.* **2006**, *18*, 15–24.
53. Kolli, R. Experimental investigation on mechanical properties of fly ash-GGBFS based GO-geopolymer concrete using mineral sand (Quartz-Feldspar) as fine aggregate. *Mater. Today Proc.* **2022**, *60*, 40–45.
54. Tian, L.; Feng, W.; Ma, H.; Zhang, S.; Shi, H. Investigation on the microstructure and mechanism of geopolymer with different proportion of quartz and K-feldspar. *Constr. Build. Mater.* **2017**, *147*, 543–549. [[CrossRef](#)]
55. Bong, S.H.; Nematollahi, B.; Xia, M.; Nazari, A.; Sanjayan, J. Properties of one-part geopolymer incorporating wollastonite as partial replacement of geopolymer precursor or sand. *Mater. Lett.* **2020**, *263*, 127236. [[CrossRef](#)]

56. Archez, J.; Texier-Mandoki, N.; Bourbon, X.; Caron, J.F.; Rossignol, S. Influence of the wollastonite and glass fibers on geopolymer composites workability and mechanical properties. *Constr. Build. Mater.* **2020**, *257*, 119511. [[CrossRef](#)]
57. Dick, A.; Bhandari, B.; Dong, X.; Prakash, S. Feasibility study of hydrocolloid incorporated 3D printed pork as dysphagia food. *Food Hydrocoll.* **2020**, *107*, 105940. [[CrossRef](#)]
58. Zhang, C.; Wang, C.S.; Therriault, D.; Heuzey, M.C. Development of aqueous protein/polysaccharide mixture-based inks for 3D printing towards food applications. *Food Hydrocoll.* **2022**, *131*, 107742. [[CrossRef](#)]
59. Aboulayt, A.; Jaafri, R.; Samouh, H.; El Idrissi, A.C.; Roziere, E.; Moussa, R.; Loukili, A. Stability of a new geopolymer grout: Rheological and mechanical performances of metakaolin-fly ash binary mixtures. *Constr. Build. Mater.* **2018**, *181*, 420–436. [[CrossRef](#)]
60. Chang, I.; Im, J.; Prasadhi, A.K.; Cho, G.C. Effects of Xanthan gum biopolymer on soil strengthening. *Constr. Build. Mater.* **2015**, *74*, 65–72. [[CrossRef](#)]
61. Gao, H.; Qing, L.; Ma, G.; Zhang, D.; Wei, C. Numerical investigation into effects of rheological properties on grout flow in rock fracture using Herschel-Bulkley model. *Eng. Geol.* **2024**, *329*, 107402. [[CrossRef](#)]
62. Mizuno, H.; Ikeda, A.; Kawasaki, T.; Miyazaki, K. Universal mechanism of shear thinning in supercooled liquids. *Commun. Phys.* **2024**, *7*, 199. [[CrossRef](#)]
63. Rosti, M.E.; Takagi, S. Shear-thinning and shear-thickening emulsions in shear flows. *Phys. Fluids* **2021**, *33*, 083319. [[CrossRef](#)]
64. Schwab, A.; Levato, R.; D'Este, M.; Piluso, S.; Eglin, D.; Malda, J. Printability and shape fidelity of bioinks in 3D bioprinting. *Chem. Rev.* **2020**, *120*, 11028–11055. [[CrossRef](#)] [[PubMed](#)]
65. Panda, B.; Unluer, C.; Tan, M.J. Extrusion and rheology characterization of geopolymer nanocomposites used in 3D printing. *Compos. Part B Eng.* **2019**, *176*, 107290. [[CrossRef](#)]
66. Mewis, J.; Wagner, N.J. Thixotropy. *Adv. Colloid Interface Sci.* **2009**, *147*, 214–227. [[CrossRef](#)]
67. Prabhakar, S.; Rao, K.H.; Forsling, W. Dissolution of wollastonite and its flotation and surface interactions with tallow-1, 3-diaminopropane (duomeen T). *Miner. Eng.* **2005**, *18*, 691–700. [[CrossRef](#)]
68. Dong, H.; Aziz, N.A.; Shafri, H.Z.M.; Ahmad, K.A.B. Computational fluid dynamics study on cemented paste backfill slurry. *Constr. Build. Mater.* **2023**, *369*, 130558. [[CrossRef](#)]
69. Brady, J.F. The rheological behavior of concentrated colloidal dispersions. *J. Chem. Phys.* **1993**, *99*, 567–581. [[CrossRef](#)]
70. Brader, J.M. Nonlinear rheology of colloidal dispersions. *J. Phys. Condens. Matter* **2010**, *22*, 363101. [[CrossRef](#)]
71. Gholamipour-Shirazi, A.; Norton, I.T.; Mills, T. Designing hydrocolloid based food-ink formulations for extrusion 3D printing. *Food Hydrocoll.* **2019**, *95*, 161–167. [[CrossRef](#)]
72. Baniasadi, H.; Kimiaei, E.; Polez, R.T.; Ajdary, R.; Rojas, O.J.; Österberg, M.; Seppälä, J. High-resolution 3D printing of xanthan gum/nanocellulose bio-inks. *Int. J. Biol. Macromol.* **2022**, *209*, 2020–2031. [[CrossRef](#)] [[PubMed](#)]
73. Avery, M.P.; Klein, S.; Richardson, R.; Bartlett, P.; Adams, G.; Dickin, F.; Simske, S. The rheology of dense colloidal pastes used in 3D-printing. In Proceedings of the Nip & Digital Fabrication Conference, Philadelphia, PA, USA, 7–11 September 2014; Society for Imaging Science and Technology: Springfield, IL, USA, 2014; Volume 1, pp. 140–145.
74. Quemada, D.; Berli, C.L.A. *Interactions Dans Les Dispersions; Stabilisation*; Lavoisier: Paris, France, 2006.
75. Kröger, M.; Vermant, J. *The Structure and Rheology of Complex Fluids*; Oxford University Press: Oxford, UK, 2000.
76. Suiker, A.S.; Wolfs, R.J.; Lucas, S.M.; Salet, T.A. Elastic buckling and plastic collapse during 3D concrete printing. *Cem. Concr. Res.* **2020**, *135*, 106016. [[CrossRef](#)]

Disclaimer/Publisher's Note: The statements, opinions and data contained in all publications are solely those of the individual author(s) and contributor(s) and not of MDPI and/or the editor(s). MDPI and/or the editor(s) disclaim responsibility for any injury to people or property resulting from any ideas, methods, instructions or products referred to in the content.